

# The next generation Birmingham Solar Oscillations Network (BiSON) spectrophotometer: a new miniaturised instrument for helioseismology

S. J. Hale,<sup>1</sup><sup>\*</sup> W. J. Chaplin,<sup>1</sup> G. R. Davies,<sup>1</sup> Y. P. Elsworth,<sup>1</sup> R. Howe,<sup>1</sup>

<sup>1</sup>*School of Physics and Astronomy, University of Birmingham, Edgbaston, Birmingham B15 2TT, United Kingdom*

Accepted XXX. Received YYY; in original form ZZZ

## ABSTRACT

We describe a new spectrophotometer for the Birmingham Solar Oscillations Network (BiSON), based on a next generation observation platform, BiSON:NG, a significantly miniaturised system making use of inexpensive consumer-grade hardware and off-the-shelf components, where possible. We show through system modelling and simulation, along with a summer observing campaign, that the prototype instrument produces data on the Sun’s low-degree acoustic (p-mode) oscillations that are of equal quality and can be seamlessly integrated into the existing network. Refreshing the existing ageing hardware, and the extended observational network potential of BiSON:NG, will secure our ongoing programme of high-quality synoptic observations of the Sun’s low-degree oscillations (e.g., for seismic monitoring of the solar cycle at a “whole Sun” level).

**Key words:** Instrumentation – instrumentation: photometers – techniques: spectroscopic – techniques: radial velocities – Sun: helioseismology – Sun: activity

## 1 INTRODUCTION

The Birmingham Solar Oscillations Network (BiSON) observes acoustic oscillations of the Sun-as-a-star, via a network of ground-based automated telescopes (Brookes 1974; Brookes et al. 1978; Hale et al. 2016; Hale 2019). The observed modes are of low angular degree, and provide data for characterising the solar activity cycle at the “whole Sun” level (see, e.g., Chaplin et al. 2019; Howe et al. 2022), and the structure and dynamics of the deep solar interior. The network is composed of six sites – Mount Wilson, Los Angeles, USA; Las Campanas, Chile; Izaña, Tenerife, Canary Islands; Sutherland, South Africa; Carnarvon, Western Australia; and Narrabri, New South Wales, Australia. Four of the sites are fully automated and use a 4 metre observatory dome and a large equatorial mount. Two of the sites, Mount Wilson and Izaña, collect light via a cœlostad and so require observers. In this paper, we describe a new instrument based on a next generation observation platform, BiSON:NG (Hale et al. 2020), a significantly miniaturised system making use of inexpensive consumer-grade hardware and off-the-shelf components (Hale 2019).

The miniaturised system separates the collection optics from the instrument via an optical fibre, and so requires only a small amateur telescope mount and small enclosure, which can be inexpensively installed on the roof of existing infrastructure. Moving the instrumentation off a mount and away from direct sunlight improves thermal stability and robustness of the data. Use of off-the-shelf hardware, where possible, simplifies the design, operation, and reduces cost in comparison with bespoke construction. Ensuring that several sources of similar or ideally identical components exists removes a supplier

single-point failure, and helps maintenance requirements particularly on long term projects.

In Section 2 we give an overview of the operation of the instrument, and model the expected performance. In Section 3 we analyse sources of noise that contribute to the expected overall white noise background level, and in Section 4 describe how data are acquired and recorded. Finally, in Section 5, we show initial results from a prototype trial during 2018 at Izaña.

## 2 A MINIATURE SPECTROPHOTOMETER

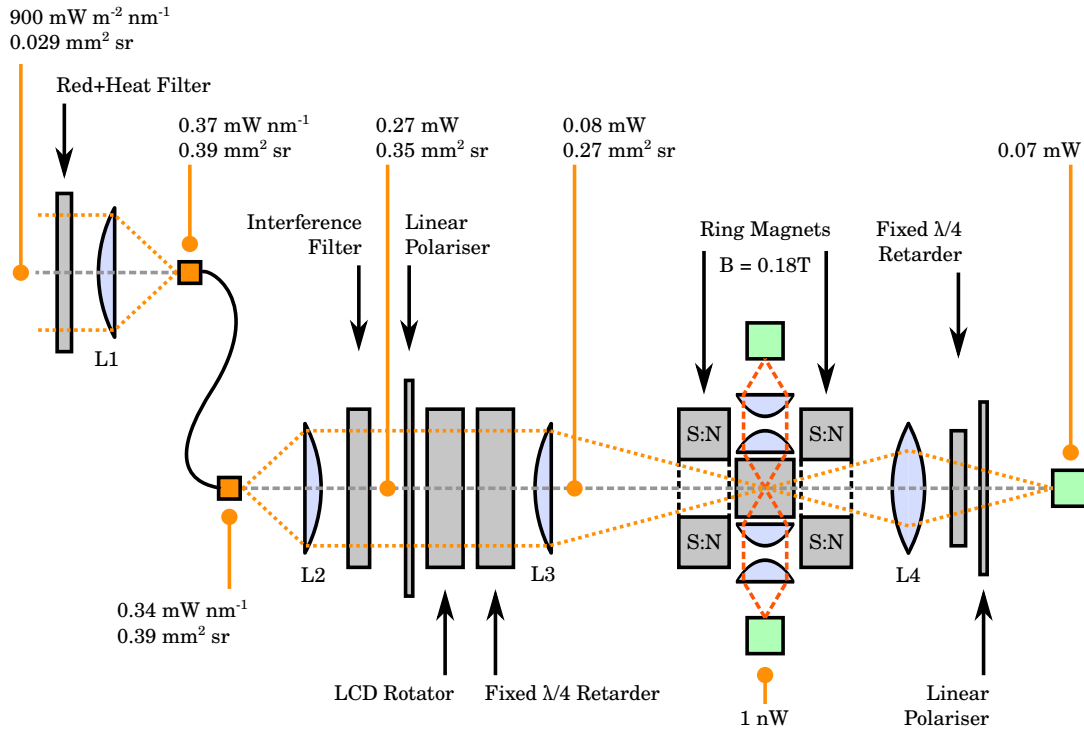
All BiSON instruments are resonance scattering spectrophotometers (RSS). Light scattered from a potassium vapour cell is used to make high-precision photometric measurements of the Doppler velocity of the solar surface, by observing fluctuations in the intensity of the D1 transition at 769.898 nm. The original BiSON spectrophotometer is described in detail by Brookes (1974) and Brookes et al. (1978). The design philosophy has changed little over the years, with differences only in the type of chassis and style of magnet/oven assembly.

Figure 1 shows an optical schematic of the new miniaturised fibre-fed spectrophotometer. Over the next few subsections we describe an end-to-end system model, from the objective optics, through optical signal processing, to the final detectors.

### 2.1 Optical Power Budget

We start by considering the power available at the entrance to the instrument. The solar constant is  $1365 \text{ W m}^{-2}$ , measured at the top of Earth’s atmosphere, and the contribution to this near our target wavelength of 770 nm is  $1.22 \text{ W m}^{-2} \text{ nm}^{-1}$ . To determine the power

\* E-mail: s.j.hale@bham.ac.uk



**Figure 1.** Schematic of a fibre-based BiSON resonance scattering spectrophotometer. The étendue and optical power (or power spectral density, as appropriate) is indicated at key points in the system by the orange markers. The green boxes indicate detector locations - two perpendicular to the optical axis detecting light scattered from the vapour cell, and one detecting the light transmitted directly through the cell.

reaching the ground we must take into account atmospheric extinction.

At 770 nm atmospheric extinction is dominated by the contribution of aerosols. The aerosol optical depth at the BiSON site at Las Campanas, Chile, is typically 0.03 magnitudes per airmass, whereas the BiSON site at Izaña, Tenerife, can reach as high as 0.5 magnitudes per airmass during periods of high Saharan dust (Hale et al. 2017). At one airmass with an aerosol optical depth of 0.03, the power spectral density at sea level near 770 nm is  $1.18 \text{ W m}^{-2} \text{ nm}^{-1}$ . If we estimate six airmasses with an aerosol optical depth of 0.1, the typical maximum value outside of periods of high Saharan dust, this reduces the power spectral density at sea level to  $0.67 \text{ W m}^{-2} \text{ nm}^{-1}$ . When modelling system response, we assume an optical power spectral density budget of  $0.9 \text{ W m}^{-2} \text{ nm}^{-1}$  as a nominal mid-range value.

## 2.2 Objective Optics

A deep-red filter is the first element in the system, and is used to relieve much of the infra-red thermal load on the instrument. Historically, this has been a combination of a Schott RG9 at 3 mm thickness, and a Schott KG4 at 1 mm thickness, giving a combined transmission of 70% at 770 nm. Schott KG4 has been discontinued and is obsolete. The most common filter set in use today is the photometric system designed by Fukugita et al. (1996) for the Sloan Digital Sky Survey (SDSS). The SDSS i'2 filter is an ideal replacement, with a bandwidth of 695 nm to 844 nm providing better infra-red rejection, and transmission at 770 nm of 98%. Figure 2 shows the profile of the SDSS i'2 filter, and the combined RG9+KG4 profile.

Objective lens L1 has 25.4 mm diameter and 30 mm focal length. The solar field angle at perihelion is  $0.542^\circ$ , and this is the minimum acceptance angle required to view the whole extent of the solar disc. Lens L1 projects a 0.6 mm image of the solar disc onto

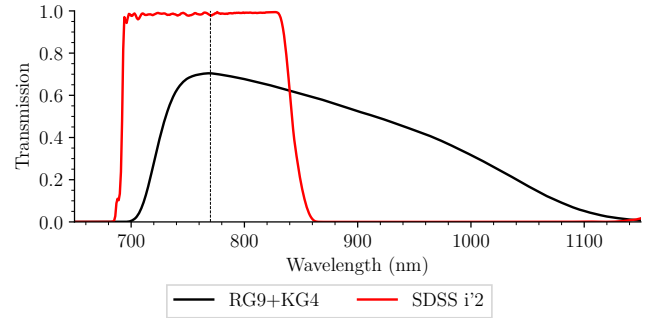


**Figure 2.** Profiles of the SDSS i'2 filter, and the original RG9+KG4 filters. The dashed vertical line indicates the 770 nm operational wavelength.

the end of an optical fibre with 1.0 mm core diameter. The image is larger than 0.3 mm predicted by first-order optics due to the fast focal ratio and imperfect correction of aberrations, but well within the acceptance of the fibre. The lens clear aperture is 22.8 mm collecting  $0.37 \text{ mW nm}^{-1}$  based on our optical power budget.

The combined collection optics are small and light enough, and have sufficient tolerance to guiding errors, to be used with any inexpensive amateur telescope mount (Hale 2019; Hale et al. 2020).

## 2.3 Fibre Coupling

A off-the-shelf 1000  $\mu\text{m}$  multimode fibre is used to couple the collection optics to the instrument. The numerical aperture is 0.39 producing an acceptance angle of  $23^\circ$ , matching the cone of light produced by the objective lens. The large core diameter was selected in order

to both improve the light throughput, and to prevent the focal ratio of the collection optics becoming unfeasibly small.

The optical fibre scrambles the image of the Sun that is focused on the input of the fibre by the collection optics. Since BiSON observes the Sun-as-a-star this is a desirable addition to the design, as it reduces sensitivity to solar rotation, instrumental vignetting, and almost completely eliminates sensitivity to guiding error. Since an image of the Sun is focused onto the end of the fibre it is essential, as with all optics in a focal plane, that the fibre end remains completely clean and undamaged. A piece of dust or dirt on the fibre end would cause variable transmission across the input, and then motion of the solar image due to guiding errors would cause different parts of the solar image to be preferentially transmitted. The objective lens and fibre connection are sealed inside an optical tube assembly.

The fibre output is collimated by lens L2, with the same properties as the objective lens L1. The collimated beam through the instrument has a diameter of 22.8 mm and divergence of  $1^\circ$ . The power entering the spectrophotometer is estimated at  $0.34 \text{ mW nm}^{-1}$ . Due to the beam divergence there is some vignetting through the instrument, and this is minimised by ensuring all components are as close together as possible. Since the beam is uniform after passing through the optical fibre, the small amount of vignetting is simply a loss of power rather than a loss of information.

## 2.4 Optical Signal Processing

The first stage of optical signal processing is an interference filter with 1.5 nm bandwidth. This is used to isolate the potassium D1 absorption line at 770 nm from the nearby D2 absorption line at 766 nm, which is heavily contaminated by atmospheric effects.

The potassium vapour cell is placed in a longitudinal magnetic field which causes the line to be Zeeman-split into two components, where the separation is dependent on the magnetic field strength. The two components of the Zeeman split line interact only with circularly polarised light, and since the two components have opposite circular polarisation it allows the LCD rotator and fixed quarter-wave plate to select which component should be observed. Splitting the lab reference-frame in this way produces two working-points of measurement, and so allows discrimination between red- and blue-shift. It also moves the measurements onto the steeper parts of the wings of the solar absorption line, improving Doppler velocity sensitivity and allows measurement even during periods crossing zero line-of-sight velocity.

Lens L3 forms an image of the fibre at the centre of the vapour cell. The requirements are that the focal length is long enough to ensure the beam has converged sufficiently before entering the aperture in the side of the magnet, but short enough so as not to cause unnecessarily high magnification of the image. A large image and high divergence would increase the likelihood of direct scattering from the glass cell walls, which would easily obscure the signal from atomic scattering. A focal length of 100 mm is used, producing a 3.3 mm diameter image of the 1 mm fibre at the centre of the cell. The power entering the cell is estimated at 0.08 mW, and is now effectively monochromatic.

The data product is an intensity-normalised ratio  $R$  formed from the two instrumental passbands of light scattered from the vapour cell,

$$R = \frac{I_b - I_r}{I_b + I_r}, \quad (1)$$

where  $I_b$  and  $I_r$  are the intensities measured at the blue and red wings of the solar absorption line, respectively. This ratio is closely

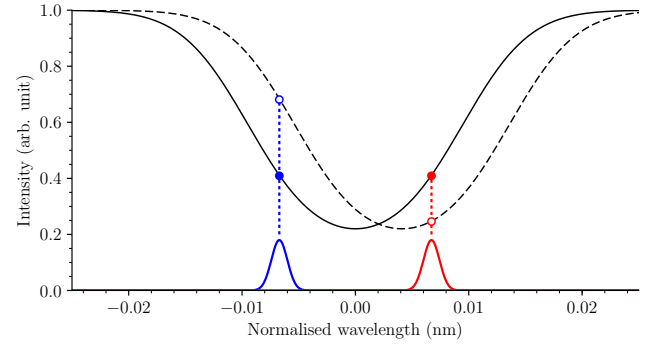


**Figure 3.** The potassium solar absorption line is shown with both zero line-of-sight velocity (solid line), and also red-shifted by  $1600 \text{ m s}^{-1}$  (dashed line) to demonstrate the effect on the scattering intensity. The two absorption components are split by a 0.18 T longitudinal magnetic field producing a separation of approximately 0.013 nm, or  $5.2 \text{ km s}^{-1}$  in terms of Doppler velocity.

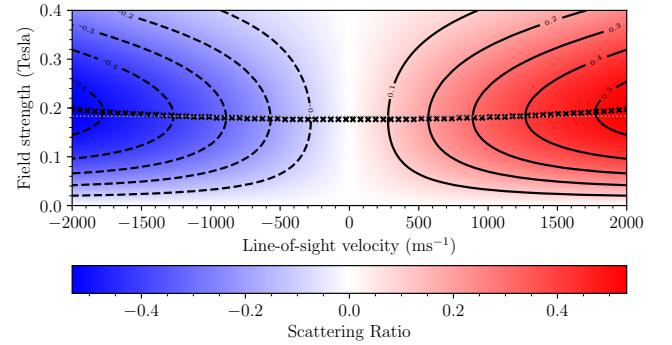


**Figure 4.** Magnetic field strength optimisation. The crosses indicate the point of maximum ratio for each velocity and therefore the ideal magnetic field strength. The faint horizontal grey dotted line indicates the mean ideal field strength of 0.18 T.

related to the Earth-Sun line-of-sight velocity, and can be calibrated according to [Elsworth et al. \(1995\)](#) and [Davies et al. \(2014\)](#).

## 2.5 Vapour Cell and Magnetic Field Strength

The potassium D1 absorption line profile is shown in Figure 3, modelled according to [Underhill \(1993\)](#). The solar line-of-sight velocity shifts between approximately  $-300 \text{ m s}^{-1}$  to  $1600 \text{ m s}^{-1}$  over one year, and this gives lower and upper bounds on the acceptable magnetic field strength.

The lower limit to the applied magnetic field is set by the requirement that the red and blue components are both fully separated, and always on opposite sides of the line at all line-of-sight velocities. The upper limit is set by the blue component moving completely off the absorption line and into the continuum at maximum offset. The potential range of magnetic field strength is therefore between 0.1 T to 0.3 T.

Figure 4 shows the predicted scattering ratio over a range of velocity offsets and magnetic field strengths, drawn symmetrically for completeness. The ideal field strength maximising velocity sensitivity is 0.18 T, which splits the two components by 0.013 nm, or  $5.2 \text{ km s}^{-1}$  in terms of Doppler velocity.

Figure 5 shows the magnet and cell oven assembly. It is possible to

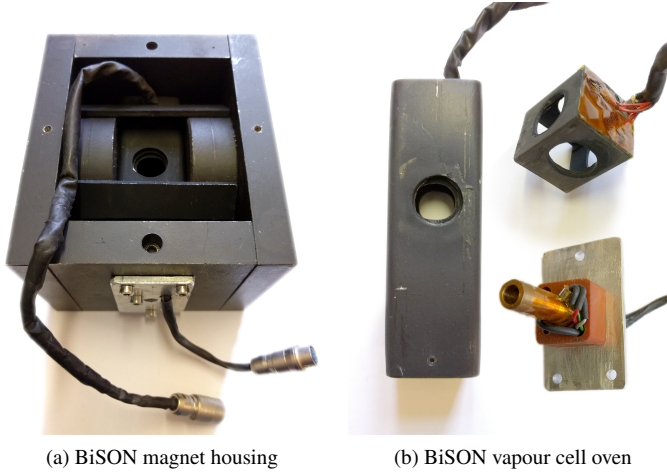


**Figure 5.** An example BiSON magnet and vapour cell oven. (a) shows the magnet and yoke, with the cell oven installed inside. (b) shows the cell oven, including the separate cube and stem heaters.

estimate the power reaching the scattering detectors by considering the geometry of the cell, the scattering cross section, and the collection optics. The scattering intensity is maximised at a cell stem temperature of approximately 80 °C to 90 °C, at which temperature the optical depth is approximately unity when measured from the front of the cell to the centre (Hale et al. 2020a). We first scale by,

$$I_1 = I_0 e^{-1}, \quad (2)$$

making an assumption of single-scattering. This is acceptable since we require only a simple power estimate. We then scale by the scattering cross-section,

$$I_2 = I_1 \frac{\lambda_{cs}}{\lambda_{beam}}, \quad (3)$$

where  $\lambda_{cs}$  is the scattering cross-section of approximately 4 pm and  $\lambda_{beam}$  is the incoming beam bandwidth of approximately 1 nm. The cell scattering is isotropic, and so if we assume a spherical cell we can make use of the inverse square law to calculate the power incident at the collection optics,

$$I_3 = I_2 \frac{d^2}{D^2}, \quad (4)$$

where  $d$  is the image diameter at the centre of the cell of approximately 3.3 mm and  $D$  is the distance to the collection optics of approximately 9 mm. Finally we need to scale by the aperture area,

$$I_{det} = I_3 \frac{A_{det}^2}{A_{beam}^2}, \quad (5)$$

where  $A_{beam}$  is the beam aperture of approximately 20 mm and  $A_{det}$  is the detector aperture of 6 mm. The final intensity at the detector,  $I_{det}$ , is approximately 1.5 nW if measuring in the solar continuum. The solar potassium absorption line has an absorption depth of around 77 %, and so the final value is between 0.35 nW and 1.4 nW depending on the line-of-sight velocity offset. We assume a nominal 1 nW of scattering power.

## 2.6 Transmission Monitor

It is useful to monitor the light that is not scattered by the cell and is transmitted directly through the spectrophotometer. This measurement allows the quality of beam polarisation to be monitored, and

also to estimate the daily atmospheric extinction coefficient (Hale et al. 2017).

Lens L4 is a 50 mm focal length bi-convex lens positioned to focus light exiting from the cell into an image on the transmission detector, via a fixed linear polariser and quarter-wave plate. We determined that the optical power entering the vapour cell is 0.08 mW, and this can be also be considered to be the total light exiting the cell since very little power is removed from the beam by resonance scattering. The power at the transmission detector is 0.07 mW when the input and output polarisation of the whole system is uncrossed, and essentially zero when crossed. The filters and the photodiode are mounted with a small wedge angle in order to prevent back-reflections into the cell.

## 3 NOISE SOURCES

The noise characteristics of RSS instruments have been investigated by several authors in terms of time-dependent effects on the science extracted from the observations – see, e.g., Grec et al. (1976); Brookes et al. (1978); Appourchaux (1989); Hoyng (1989, 1991); Chaplin et al. (2005). Here, we consider the contributions to noise on the whole envelope.

### 3.1 Atmospheric Scintillation

The effect of atmospheric scintillation on the measured intensity has a maximum of around  $15 \text{ nW } \sqrt{\text{Hz}}^{-1}$  (Hale et al. 2020b), and this is the dominant noise source. The  $-3 \text{ dB}$  point (noise power reduced to 50 %) typically occurs at around 5 Hz, and the  $-6 \text{ dB}$  point (noise power reduced to 25 %) typically occurs at between 5 Hz to 15 Hz. The  $-10 \text{ dB}$  point (noise power reduced to 10 %) typically occurs above 20 Hz (Hale et al. 2020b).

BiSON instrumentation reduces the effect of scintillation noise by forming a velocity ratio from the measurements of the two working points on the solar absorption line. The level of noise reduction is determined by how quickly the system can switch between polarisation states – faster switching requires shorter exposure times, with observation of each wing closer to being simultaneous, and the instrument “sees” less atmospheric turbulence.

The original Mark-I instrument switches at 0.5 Hz and little of the atmospheric scintillation is eliminated. Newer BiSON instrumentation uses a bespoke Pockels-effect cell and drive electronics to achieve a switching rate of 90.9 Hz, with 15 % dead time due to stabilisation delays and data readout within each integration period. At this switching rate the atmospheric scintillation power has decayed below 10 % and is less than  $5 \text{ nW } \sqrt{\text{Hz}}^{-1}$ .

We saw earlier that the new miniature instrument uses an off-the-shelf LCD to control polarisation state. The LCD rotator requires up to 27 ms to change state (Hale et al. 2022, submitted), and so a switching rate of around 5 Hz can be obtained with dead time of 20 %. This can be increased to around 10 Hz with 50 % dead time. Due to the slower switching rate we can expect the white noise level due to atmospheric scintillation to rise to between  $7.5 \text{ nW } \sqrt{\text{Hz}}^{-1}$  to  $10 \text{ nW } \sqrt{\text{Hz}}^{-1}$ , depending on natural daily variability.

### 3.2 Guiding Noise

In traditional BiSON instrumentation where the Sun is imaged inside the vapour cell, an additional source of noise is caused by guider errors. Guider fluctuations cause the image of the Sun to move around inside the vapour cell, which changes the vapour optical depth seen

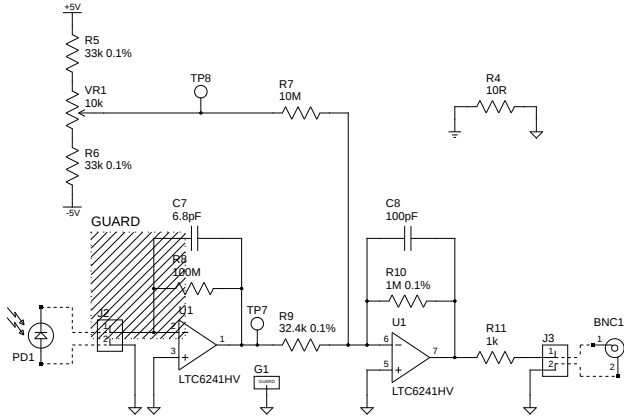


**Figure 6.** Scattering detector transimpedance amplifier schematic.

by the scattering detectors, and this in turn causes changes in the measured velocity ratio. It is difficult to determine a quantitative measure of this effect.

As discussed earlier, the new instrument focuses an image of the Sun onto the end of an optical fibre. The output of the fibre is uniform regardless of the absolute position of the image provided that the image falls entirely within the core of the fibre. The constraint on guiding accuracy is relaxed and guider noise is considered to be eliminated completely, so long as the error is not so large as to cause vignetting.

### 3.3 Electronic Noise

There are two scattering detectors, one on each side of the cell perpendicular to the beam. We saw earlier that the expected optical intensity is between 0.35 nW and 1.4 nW. The detectors use a photodiode with responsivity at 770 nm of  $0.45 \text{ A W}^{-1}$ . The expected photocurrent is of the order of 160 pA to 630 pA, which requires high amplification to raise the signal to a suitable level for the input to the digitizers. In comparison to the five minute solar oscillations, relatively high bandwidth of a few hundred Hz is also required due to multiplexing multiple polarisation states creating transient signal state changes. The amplifier schematic itself is relatively simple, shown in Figure 6. However, with such high impedance circuits great care must be taken in the design and construction to ensure the expected performance levels are achieved.

An amplifier with low noise characteristics was selected for both amplification stages. The input bias current typical value is just 0.2 pA, the input noise is  $0.56 \text{ fA } \sqrt{\text{Hz}}^{-1}$ , and it has a low temperature coefficient at  $2.5 \mu\text{V } ^\circ\text{C}^{-1}$ . It is a bipolar rail-to-rail device allowing the output stage to swing within 30 mV of either supply rail and so maximise the signal dynamic range. A total of three different grounds are defined in the circuit to isolate the signal from noise sources as much as possible. The sensitive high-impedance connection between the photodiode output and the inverting input of the transimpedance amplifier is protected by a low-impedance signal guard ring. The soldermask is removed from this section of the board to avoid creating a leakage bridge over the guard ring. This is essential to limit noise, since even a  $10 \text{ G}\Omega$  resistance across the PCB between a 5 V supply trace and a high-impedance input would add 500 pA of leakage current – equal to the signal we are trying to amplify and three orders of magnitude higher than the input bias current of the operational amplifier.

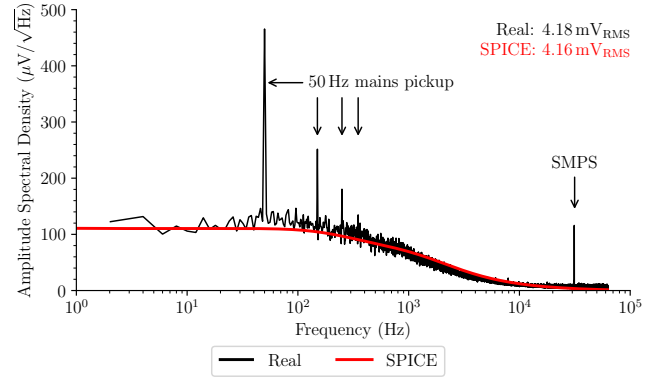


**Figure 7.** Measured scattering detector noise, along with the expected noise profile from SPICE simulation. The physical detector suffers from some minor mains pickup at 50 Hz, and a peak around 30 kHz due to powering the detector from a switched-mode power-supply (SMPS), but broadly matches expectation.

The noise performance of the detector was simulated using SPICE, the industry standard electrical simulation tool (Nagel & Pederson 1973; Nagel 1975). Figure 7 shows the simulated detector in red, and data from the real detector in black. The real detector suffers from some slight mains pickup at 50 Hz, and the peak around 30 kHz is due to powering the detector from a switched-mode power-supply. The noise level is minor and the performance matches expectation. The RMS noise amplitude is approximately 4.2 mV<sub>RMS</sub>. The typical noise value of  $100 \mu\text{V } \sqrt{\text{Hz}}^{-1}$  can be rescaled by the amplifier gain enabling the noise equivalent power (NEP) to be calculated. This is the equivalent signal that would be required to produce the same output from an ideal noiseless detector. The electronic NEP is  $0.07 \text{ pW } \sqrt{\text{Hz}}^{-1}$ , several orders of magnitude less than that due to atmospheric scintillation.

The bandwidth –3 dB point (noise power reduced to 50 %) occurs at 239 Hz, producing a slew duration of about 4 ms which is sufficient to pass the transient changes that occur during LCD polarisation state changes.

### 3.4 Photon Shot Noise

The typical incident flux on the scattering detectors is of the order of 1 nW. For 1 nW of light at 770 nm this is equivalent to approximately  $4 \times 10^9$  photons per second. The standard deviation of shot noise is equal to the square-root of the average number of events, and converting this back to power gives a value of  $0.02 \text{ pW}_{\text{RMS}}$ . At the detector output this is  $0.03 \text{ mV}_{\text{RMS}}$ , two orders of magnitude smaller than the electronic noise.

### 3.5 Thermal Noise

The performance of various stages of the the instrument are sensitive to their operating temperature. We actively control the working temperature of the the potassium cell stem and cube, the LCD rotator, and the two scattering photodiodes. The narrow-band interference filter is thermally stabilised on traditional BiSON instrumentation, in order to limit intensity changes resulting from movement of the passband and spectral fringes. When the instrument is operated in a thermally controlled environment and separated from the collection optics in direct sunlight, precise thermal control of filters is not required.

**Table 1.** Velocity-calibrated white noise level and noise equivalent velocity (NEV) for four BiSON spectrophotometers, and comparison with the miniature prototype instrument.

Site	FOM	Background Noise ( $\text{ms}^{-1}$ ) <sup>2</sup> Hz <sup>-1</sup>	Noise Equivalent Velocity cm s <sup>-1</sup> RMS
Mount Wilson	82.6	1.6	14.2
Sutherland	42.9	4.3	23.1
<b>BiSON:NG</b>	19.6	9.9	35.2
Narrabri	27.9	10.4	36.1
Las Campanas	25.0	13.5	41.1
Mark-I	5.5	61.6	87.7

The vapour cell has the most significant thermal contribution to the noise. Variations in the vapour cell stem temperature introduce changes in the vapour temperature, and this affects the scattering intensity due to changes in the vapour optical depth.

The temperature control system can achieve a mean stem temperature of 90 °C with a standard deviation of  $0.7 \times 10^{-3}$  °C. Using the vapour cell model from Hale et al. (2020a) this can be converted into scattering intensity noise. Assuming a detector aperture of 6 mm and scaling for a typical 1 nW intensity, the effect of thermal noise on the vapour cell is  $0.2 \text{ pW } \sqrt{\text{Hz}}^{-1}$ , which is of a similar order to the electronic noise.

#### 4 DATA ACQUISITION

The data acquisition system is based around a number 24-bit delta-sigma ( $\Delta\Sigma$ ) analogue to digital converters. The ADCs are an integrated package containing a programmable gain amplifier (PGA), a second-order  $\Delta\Sigma$  modulator, a programmable digital low-pass filter, and a micro-controller with several control registers.

The  $\Delta\Sigma$  modulator over-samples at high rate, and the rate is then reduced by the internal digital low-pass filter. This means that the digital quantisation noise is pushed up to higher frequencies and then removed by the low-pass decimation filter producing an effect known as noise shaping. The ADC can be considered to be effectively noiseless.

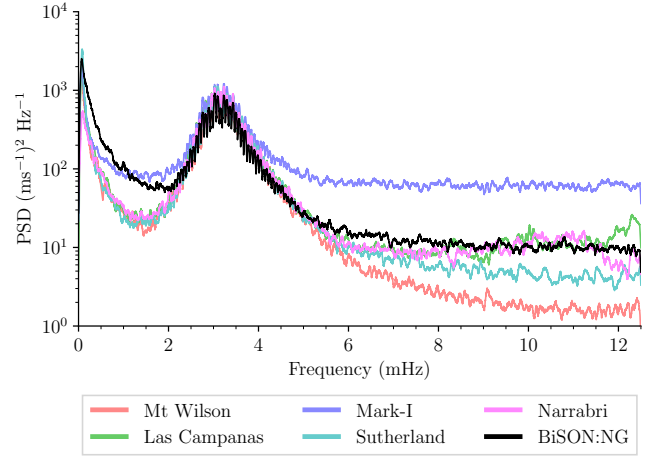
Data are read-out by a Raspberry Pi single-board computer over the on-board Serial Peripheral Interface (SPI) bus. The Raspberry Pi is a small single-board computer based around a Broadcom System-on-a-Chip (SoC) with an integrated ARM compatible CPU, and runs a version of the GNU/Linux operating system. An SoC paired with the integrated PGA, modulator, and low-pass filter, allows the whole acquisition system to be small and self-contained.

The calibration of Doppler shift to velocity is discussed by Elsworth et al. (1995), with an improved data pipeline that includes correction for atmospheric differential extinction described by Davies et al. (2014). The subsequent concatenation of data from multiple sites is discussed by Chaplin et al. (1997) and Hale (2003, 2019).

#### 5 PROTOTYPE COMMISSIONING

The prototype system was trialled at Izaña, Tenerife, over two site visits in 2017. Light from the cœlostât supplying Mark-I was shared with the new system. The instrumentation continued to run alongside Mark-I capturing contemporaneous data through summer 2018.

Figure 8 shows the power spectral density of concatenated time

**Figure 8.** Comparison of data from an observing campaign over summer 2018. The power spectral density has been smoothed with a 50  $\mu\text{Hz}$  moving mean to aid clarity.

series from each BiSON site for the summer 2018 observing campaign. Specifically, data from 2018 April 14 to 2018 August 26 were selected since this is the period where the secondary cœlostât mirror at Izaña is mounted in the summer position. A 50  $\mu\text{Hz}$  moving mean has been applied to smooth the results and aid clarity.

Table 1 provides a summary of the performance statistics from each site. The “FOM” is a signal-to-noise figure-of-merit. The signal is estimated as the mean power in the 2 mHz to 5 mHz band, and the noise background as the mean power in the upper 5.5 mHz to 12.5 mHz band. This is not perfect since there is, of course, noise within the signal band, and the upper signal cut-off is not precise. However, this definition has become a network standard metric and so it is used here for consistency and comparison. The prototype instrument achieves a background noise level of  $9.9 (\text{ms}^{-1})^2 \text{ Hz}^{-1}$ , comparable to a noise equivalent velocity RMS of  $35.2 \text{ cm s}^{-1}$ , and this is similar performance to existing full-size BiSON instrumentation.

The original Mark-I instrument has a much higher background noise level due to slower polarisation switching rate, and so it experiences much higher scintillation noise. The poorer low-frequency performance is due to the guiding accuracy of the cœlostât. The new fibre-fed instrument follows a similar low-frequency profile due to difficulty maintaining the solar image within the fibre core. In parallel with work on the new instrumentation, the spectrophotometer at Mount Wilson was also converted to fibre and is now the best performing in the network, indicated by the red line with the lowest background white noise level in Figure 8. This can be considered an example of what can be achieved when the noise reduction techniques applied here are combined with fast polarisation switching, eliminating much of the atmospheric scintillation.

#### 6 CONCLUSIONS

The aim was to develop a miniaturised spectrophotometer that required only a small amateur telescope mount, and used off-the-shelf components where possible, in order to simplify the design and maintenance requirements but without sacrificing performance. We have shown that the prototype instrument fulfils these aims, and produces data of equal quality that can be seamlessly integrated into the existing network.

Projects such as BiSON, and the extended observational network potential of BiSON:NG, provide the necessary data that probes the structure and rotation of the solar core, and continues to improve our knowledge of the dynamo that drives the solar cycle. Observation of granulation noise at different heights in the solar atmosphere, probed via different working points on the potassium D1 absorption line, is largely incoherent, and frequency regions dominated by oscillations are almost fully coherent (Lund et al. 2017). Contemporaneous observation from many sites allows exploitation of incoherence in granulation noise to beat down the observed noise level through weighted averaging of multi-working-point data (Davies et al. 2014). Such long term synoptic observations of the Sun are important for improving detection of very low-frequency modes and hence constraints on the structure of the deep solar interior.

Following a period of reduced solar activity, it is important that long-term whole-Sun seismic observations continue as we progress through Cycle 25 and into Cycle 26 in order to obtain the necessary data required to improve models of the solar dynamo. Determining the accuracy of models and predictions is also important for assessing the long-term impact on space weather. Refreshing and extending the existing ageing hardware will secure the ongoing synoptic programme of helioseismic observations of whole-Sun oscillations.

## ACKNOWLEDGEMENTS

We would like to thank all those who have been associated with BiSON over the years. We particularly acknowledge the invaluable technical assistance at all our remote network sites. During commissioning the new prototype at Izaña: Dr. Pere Pallé, Dr. Teo Roca Cortés, Antonio Pimienta, Santiago López, and all the staff at the Instituto de Astrofísica de Canarias who have contributed to running the Mark-I instrument over many years. BiSON is funded by the Science and Technology Facilities Council (STFC) grant ST/V000500/1.

## DATA AVAILABILITY

All data are freely available from the BiSON Open Data Portal – <http://bison.ph.bham.ac.uk/opendata>. Data products are in the form of calibrated velocity residuals, concatenated into a single time series from all BiSON sites. Individual days of raw or calibrated data, and also bespoke products produced from requested time periods and sites, are available by contacting the authors. Oscillation mode frequencies and amplitudes are available from Broomhall et al. (2009) and Davies et al. (2014). Source files for this document are available from the GitLab repository (Hale 2022).

## REFERENCES

- Appourchaux, T., 1989. Optimization of parameters for helioseismology experiments measuring solar radial velocities, *A&A*, **222**(1-2), 361–366.
- Brookes, J. R., 1974. *An Accurate Measurement of the Difference Between the Solar and Laboratory Wavelengths of the Sodium Resonance Lines*, Ph.D. thesis, Department of Physics, University of Birmingham, UK.
- Brookes, J. R., Isaak, G. R., & van der Raay, H. B., 1978. A resonant-scattering solar spectrometer, *MNRAS*, **185**, 1–18.
- Broomhall, A. M., Chaplin, W. J., Davies, G. R., Elsworth, Y., Fletcher, S. T., Hale, S. J., Miller, B., & New, R., 2009. Definitive Sun-as-a-star p-mode frequencies: 23 years of BiSON observations, *MNRAS*, **396**(1), L100–L104.
- Chaplin, W. J., Elsworth, Y. P., Howe, R., Isaak, G. R., McLeod, C. P., Miller, B. A., & New, R., 1997. Techniques used in the analysis of data collected by the Birmingham Solar-Oscillations Network (BiSON). II. Frequency domain analysis & data merging, *A&AS*, **125**, 195–205.
- Chaplin, W. J., Elsworth, Y., Isaak, G. R., Miller, B. A., New, R., & Pintér, B., 2005. Noise characteristics of full-disc helioseismic observations made by resonant scattering spectrometers, *MNRAS*, **359**(2), 607–614.
- Chaplin, W. J., Howe, R., Basu, S., Elsworth, Y., Milbourne, T. W., Haywood, R. D., Davies, G. R., Hale, S. J., Miglio, A., & Ross, E., 2019. Sensitivity of low-degree solar p modes to active and ephemeral regions: frequency shifts back to the Maunder minimum, *MNRAS*, **489**(1), L86–L90.
- Davies, G. R., Broomhall, A. M., Chaplin, W. J., Elsworth, Y., & Hale, S. J., 2014. Low-frequency, low-degree solar p-mode properties from 22 years of Birmingham Solar Oscillations Network data, *MNRAS*, **439**(2), 2025–2032.
- Davies, G. R., Chaplin, W. J., Elsworth, Y. P., & Hale, S. J., 2014. BiSON data preparation: a correction for differential extinction and the weighted averaging of contemporaneous data, *Monthly Notices of the Royal Astronomical Society*, **441**(4), 3009–3017.
- Elsworth, Y. P., Howe, R., Isaak, G. R., McLeod, C. P., Miller, B. A., New, R., & Wheeler, S. J., 1995. Techniques used in the analysis of solar oscillations data from the BiSON (University of Birmingham) network. I. Daily calibration., *A&AS*, **113**, 379.
- Fukugita, M., Ichikawa, T., Gunn, J. E., Doi, M., Shimasaku, K., & Schneider, D. P., 1996. The Sloan Digital Sky Survey Photometric System, *AJ*, **111**, 1748.
- Grec, G., Fossat, E., & Vernin, J., 1976. A spectrophotometer for the study of long period solar photospheric oscillations., *A&A*, **50**(2), 221–225.
- Hale, S. J., 2003. *Scientific advancements in analysis of solar oscillation data*, Master’s thesis, School of Physics and Astronomy, University of Birmingham, UK.
- Hale, S. J., 2019. *Birmingham Solar Oscillations Network: The Next Generation*, Ph.D. thesis, School of Physics and Astronomy, University of Birmingham, UK.
- Hale, S. J., 2022. The next generation Birmingham Solar Oscillations Network (BiSON) spectrophotometer: a new miniaturised instrument for helioseismology, GitLab Inc., <https://gitlab.com/drstevenhale/bison-ng-instrumentation/-/tags/v1.0>.
- Hale, S. J., Howe, R., Chaplin, W. J., Davies, G. R., & Elsworth, Y. P., 2016. Performance of the Birmingham Solar-Oscillations Network (BiSON), *Sol. Phys.*, **291**(1), 1–28.
- Hale, S. J., Chaplin, W. J., Davies, G. R., Elsworth, Y. P., Howe, R., Lund, M. N., Moxon, E. Z., Thomas, A., Pallé, P. L., & Rhodes, E. J., J., 2017. Atmospheric Extinction Coefficients in the I<sub>C</sub> Band for Several Major International Observatories: Results from the BiSON Telescopes, 1984–2016, *AJ*, **154**(3), 89.
- Hale, S. J., Chaplin, W. J., Davies, G. R., & Elsworth, Y. P., 2020. A next generation upgraded observing platform for the automated Birmingham Solar Oscillations Network (BiSON), in *Software and Cyberinfrastructure for Astronomy VI*, vol. 11452, pp. 424 – 435, International Society for Optics and Photonics, SPIE.
- Hale, S. J., Chaplin, W. J., Davies, G. R., & Elsworth, Y. P., 2020a. Modelling the response of potassium vapour in resonance scattering spectroscopy, *Journal of Physics B Atomic Molecular Physics*, **53**(8), 085003.
- Hale, S. J., Chaplin, W. J., Davies, G. R., Elsworth, Y. P., Howe, R., & Pallé, P. L., 2020b. Measurement of Atmospheric Scintillation during a Period of Saharan Dust (Calima) at Observatorio del Teide, Izaña, Tenerife, and the Impact on Photometric Exposure Times, *PASP*, **132**(1009), 034501.
- Hale, S. J., Chaplin, W. J., Davies, G. R., Elsworth, Y. P., & Howe, R., 2022. Detector bandwidth and polarisation switching rates: spectrophotometric observations of the Sun by the Birmingham Solar Oscillations Network (BiSON), *submitted*.
- Howe, R., Chaplin, W. J., Elsworth, Y. P., Hale, S. J., & Nielsen, M. B., 2022. Unexpected solar-cycle variation of acoustic mode power in Sun-as-a-star observations, *arXiv e-prints*, p. arXiv:2205.15655.
- Hoyng, P., 1989. On the Sensitivity of Resonant Scattering Spectrometers for Whole-Disk Solar Velocity Oscillation Measurements, *ApJ*, **345**, 1088.
- Hoyng, P., 1991. The velocity sensitivity of resonant scattering spectrometers

- employing a piezoelastic modulator, *Sol. Phys.*, **133**(1), 43–50.
- Lund, M. N., Chaplin, W. J., Hale, S. J., Davies, G. R., Elsworth, Y. P., & Howe, R., 2017. Spatial incoherence of solar granulation: a global analysis using BiSON 2B data, *MNRAS*, **472**(3), 3256–3263.
- Nagel, L. W., 1975. *SPICE2: A Computer Program to Simulate Semiconductor Circuits*, Ph.D. thesis, EECS Department, University of California, Berkeley.
- Nagel, L. W. & Pederson, D., 1973. SPICE (Simulation Program with Integrated Circuit Emphasis), Tech. Rep. UCB/ERL M382, EECS Department, University of California, Berkeley.
- Underhill, C. J., 1993. *An Analysis Of Possible Line-Of-Sight Velocity Effects In The Power Spectra Of Solar Oscillations*, Master's thesis, School of Physics and Space Research, University of Birmingham, UK.

This paper has been typeset from a  $\text{\LaTeX}$  file prepared by the author.